DESIGN AND PERFORMANCE OF HIGH LASER POWER INTERFEROMETERS FOR GRAVITATIONAL-WAVE DETECTION

By

KATHERINE L DOOLEY

A DISSERTATION PRESENTED TO THE GRADUATE SCHOOL
OF THE UNIVERSITY OF FLORIDA IN PARTIAL FULFILLMENT
OF THE REQUIREMENTS FOR THE DEGREE OF
DOCTOR OF PHILOSOPHY

UNIVERSITY OF FLORIDA

2011

My dedication.

ACKNOWLEDGMENTS

Some personal acknowledgements–professors, fellow grad students, friends, family.

Acknowledgments for the funding of LIGO.

This work was supported by the US National Science Foundation grants PHY-xxxxxxx and PHY-xxxxxxx to the University of Florida, Gainesville, Florida.

TABLE OF CONTENTS

LIST OF TABLES

Table | page

LIST OF FIGURES

LIST OF SYMBOLS, NOMENCLATURE, AND ABBREVIATIONS

ASC	Angular Sensing and Control
EOM	electro-optic modulator
FI	Faraday isolator
GW	gravitational wave
IO	Input Optics
LIGO	Laser Interferometer Gravitational-wave Observatory
LSC	length sensing and control
MC	mode cleaner
MMT	mode matching telescope
PSL	pre-stabilized laser
PRC	power recycling cavity
REFL	reflected beam
RF	radio frequency
RM	recycling mirror
TGG	Terbium Gallium Garnate
TM	test mass
VIRGO	Variability of Solar Irradiance and Gravity Oscillations
WFS	wave-front sensor

Abstract of dissertation Presented to the Graduate School
of the University of Florida in Partial Fulfillment of the
Requirements for the Degree of Doctor of Philosophy

DESIGN AND PERFORMANCE OF HIGH LASER POWER INTERFEROMETERS FOR GRAVITATIONAL-WAVE DETECTION

By

Katherine L Dooley

September 2011

Chair: David Reitze
Major: Physics

My abstract.

CHAPTER 1
PURPOSE OF THIS WORK

The purpose of this work is to demonstrate the capability of an interferometric gravitational wave detector to operate at several times the highest of laser powers previously used. From a naïve standpoint, more power is desirable since strain sensitivity improves by $\sqrt{P}$ in the high frequency (> 200 Hz) shot-noise-limited region. However, as detectors become more sensitive at low frequencies (< 70 Hz), radiation pressure noise will become the dominant noise source, making high laser power operation a design trade-off. Currently, seismic noise limits low frequency sensitivity, so exploring the technical world of increasing the laser power is a fruitful adventure.

Operation of Initial LIGO was limited to 7 W input power due to uncontrolled radiation pressure torque instabilities in the arm cavities. WRONG!!!. Explained theoretically by Sidles and Sigg [1], measured experimentally by Hirose [2], and modeled numerically by Barsotti [3], the effect of radiation pressure torque on angular alignment needed to be addressed in practice in order for Enhanced LIGO to succeed in operating at powers greater than 7 W. We present the re-designed Angular Sensing and Control (ASC) system as implemented on the Enhanced LIGO detectors and show results of its performance with up to 20 W input power, demonstrating good agreement between theory, experiment and model.

The use of more power also complicates interferometer operations because of thermal effects. The optics which condition the laser for use in the interferometer experienced degradation in their performance in Initial LIGO as the result of absorbing too much heat. Less absorptive optical components were chosen with the goal of conquering thermal issues at the source, and changes were made to the architecture of the Input Optics to compensate for any residual effects. We present the re-designed Input Optics and their thermal performance with up to 30 W input power.

CHAPTER 2
THE SEARCH FOR GRAVITATIONAL WAVES

The field of ground-based gravitational-wave (GW) physics is rapidly approaching a state with a high likelihood of detecting GWs for the first time. Such a detection will not only validate part of Einstein's general theory of relativity, but initiate an era of astrophysical observation of the universe through GWs. Gravitational waves are dynamical strains in space-time that travel at the speed of light and are generated by non-axisymmetric acceleration of mass. The frequency of the gravitational wave depends on its source. A first detection is expected to witness an event such as a binary black hole/neutron star merger. This chapter provides the theoretcial framework of gravitational wave generation and presents various ways to detect them, including the current status of an effort to do so.

2.1 The theory of gravitational radiation

Gravitational radiation is a perturbation $|h_{\mu\nu}| \ll 1$ to the flat space-time Minkowski metric $\eta_{\mu\nu} = \mathrm{diag}(-1,1,1,1)$. The metric describing space-time in the presence of gravitational radiation is therefore

$$g_{\mu\nu} = \eta_{\mu\nu} + h_{\mu\nu}. \tag{2.1.1}$$

Just as in electrodynamics where one has freedom in choosing the vector potential $\vec{A}$ for calculating the magnetic field $\vec{B} = \vec{\nabla} \times \vec{A}$, one also has freedom in general relativity in choosing the form of $h_{\mu\nu}$ for ease of calculation. A convenient and popular choice is called the transverse-traceless (TT) gauge in which

$$h_{\mu\nu} = \left[\!\left[\begin{array}{cccc} 0 & 0 & 0 & 0 \\ 0 & h_+ & h_\times & 0 \\ 0 & h_\times & -h_+ & 0 \\ 0 & 0 & 0 & 0 \end{array} \right]\!\right] \tag{2.1.2}$$

where the $+$ and $\times$ represent two linearly independent polarizations. Without loss of generality, we consider the h_+ polarization in the example that follows.

For a gravitational wave traveling along the z axis, the metric is given by:

$$ds^2 = -c^2dt^2 + [1 + h_+(t)]dx^2 + [1 - h_+(t)]dy^2. \tag{2.1.3}$$

This says the TT coordinate system is stretched along the x axis and and compressed along the y axis by a factor of

$$\sqrt{1 \pm h_+(t)} \approx 1 \pm \frac{1}{2}h_+(t). \tag{2.1.4}$$

Therefore, the *proper distance* between two free masses located along either the x or the y axes changes by the factor in Eq. 2.1.4; their coordinate separations remain constant. The GW perturbation is a dimensionless strain

$$h = 2\frac{\Delta L}{L}. \tag{2.1.5}$$

2.2 Sources

Any object with an accelerating mass quadrupole moment generates gravitational waves. The typical strain amplitudes, however, are extremely tiny: a binary system of coalescing $1M_\odot$ neutron stars in the Virgo Cluster (a distance of 15 Mpc) would produce a maximum GW strain on Earth of only 10^{-21}. The strain is proportional to source mass and velocity, and inversely proportional to distance from the observer:

$$h \approx \frac{GMv^2}{Rc^4} \tag{2.2.1}$$

Consequently, the most promising sources of detectable gravitational waves are nearby, fast-moving, massive astrophysical objects that include

- supernovae
- binary stars (orbiting or coalescing)
- spinning neutron stars
- cosmological/astrophysical background

and can be categorized as producing periodic, burst, or stochastic GWs.

Stably orbiting binary star systems comprised of black holes or neutron stars as well as rapidly spinning non-axisymmetric pulsars are considered periodic sources since they will produce GWs of relatively constant frequency. These reliable sources of GWs require a long integration time to pick out their signal above noise. The Hulse-Taylor binary, for instance, falls into this category. Supernovae are burst sources since the gravitational collapse will produce a short-lived, unmodeled emission of GWs. Binaries in their final tens of milliseconds of inspiral also fall into this category. Finally, the anisotropies in the inflation of the universe together with the hum of all distant astrophysical sources will create a stochastic background of radiation. Coherent cross-correlation between multiple detectors is necessary for measuring the constant amplitude, broad-spectrum GW background.

Directly detecting gravitational radiation from any such source will reveal information that electromagnetic radiation cannot convey. The frequency of the GW tells about the dynamical timescale of the source. Only through GW radiation, for example, can mass and spin properties of a black hole be revealed.

2.3 Methods of detection

- Hulse/Taylor
- Resonant bars
- Pulsar timing
- CMB polarization (B-modes)
- Interferometry

For an approachable overview of the history of the field, including detector design choices and estimated GW strain amplitudes of various sources, refer to Ref. [4].

2.4 State of ground-based interferometry

A network of first generation kilometer scale laser interferometer gravitational-wave detectors completed its integrated 2-year data collection run in 2007, called S5. The instruments were: the American Laser Interferometer Gravitational-wave Observatories (LIGO)[5], one in Livingston, LA with 4 km long arms and two in Hanford, WA with 4 km and 2 km long arms; the 3 km French-Italian detector VIRGO[6] in Cascina, Italy; and the 1.2 km German-British

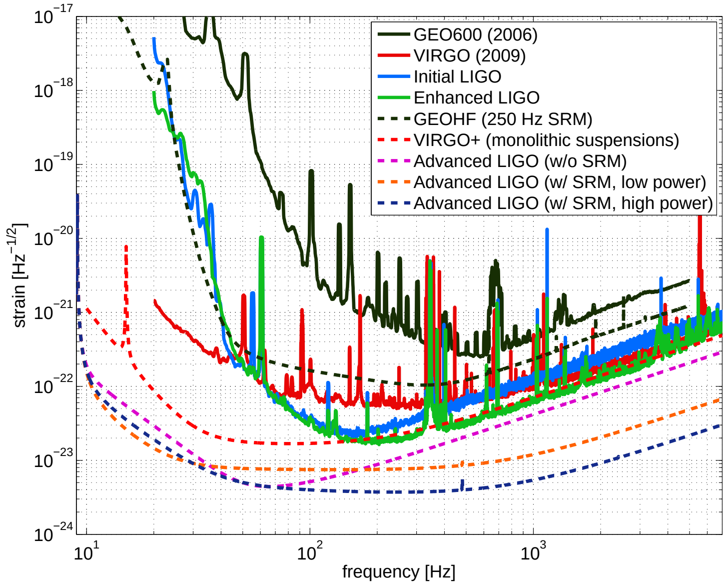

Figure 2-1. Strain sensitivities of LIGO-VIRGO collaboration interferometers.

detector GEO[7] in Ruthe, Germany. Multiple separated detectors increase detection confidence through signal coincidence and improve source localization through triangulation.

The first generation of LIGO, known as Initial LIGO, achieved its design goal of sensitivity to GWs in the 40 Hz - 7000 Hz band which included an impressive record strain sensitivity of $2 \times 10^{-23}/\sqrt{\mathrm{Hz}}$ at 155 Hz. However, only the loudest of sources produce enough GW strain to appear in LIGO's band, and no gravitational wave has yet to be found in the S5 data. A second generation of LIGO detectors, Advanced LIGO, has been designed to be at least an order of magnitude more sensitive at several hundred Hz and above and include an impressive increase in bandwidth down to 10 Hz, dramatically increasing the chances of detection. To test some of Advanced LIGO's new technologies, an incremental upgrade to the detectors was carried out after S5 [8]. This project, Enhanced LIGO, culminated with the S6 science run from July 2009 to October 2010. Currently, construction of Advanced LIGO is underway. VIRGO and GEO will both undergo their own upgrades as well [6] [9]. See Figure 2-1 for achieved and theoretical noise curves.

The baseline Advanced LIGO design [10] improves upon Initial LIGO by featuring better seismic isolation, the addition of a signal extraction mirror at the output port, homodyne readout, and an increase in laser power from 10 W to 200 W. The substantial increase in laser power improves the shot-noise-limited sensitivity, but introduces a host of radiation pressure and thermally induced side effects that must be addressed for proper operation.

The recently completed Enhanced LIGO tested portions of the Advanced LIGO designs so unforeseen difficulties could be addressed and so that a more sensitive data taking run could take place. An output mode cleaner was designed, built and installed, and DC readout of the GW signal was implemented [11]. An Advanced LIGO active seismic isolation table was also built, installed, and tested [12]. In addition, the 10 W Initial LIGO laser was replaced with a 35 W laser [13]. Accompanying the increase in laser power, the test mass Thermal Compensation System [14], the Alignment Sensing and Control, and the Input Optics were modified. The upgrades of the latter two subsystems make up the content of this dissertation.

CHAPTER 3
LASER INTERFEROMETERS FOR GRAVITATIONAL-WAVE DETECTION

3.1 Signal versus noise

The factors that must be considered in the design of any detector can be grouped into two categories: signal and noise. The ability to make a claim of detection is largely dependent on the magnitude of the signal to noise ratio (SNR). An SNR of 8 is desired for detection confidence in LIGO. For laser interferometers, the strength of the GW signal is proportional to the length of the arms and the amount of power in the arms. (See Eq. **??**.) The change in the distance between the mirrors, ΔL, is bigger for a given strain the longer the arms. And with more circulating power, the greater the amount of power that will show up at the AS port for a given displacement from the dark fringe. Therefore, the two fundamental ways to make a GW produce a bigger signal in an interferometer are: 1) make the arms longer, and 2) increase the circulating power.

No matter how large a signal one might have, it won't be found confidently, or at all, if there is too much noise. The noise itself is best grouped into categories of displacement noise and sensing noise which affect the length of the arms and the measurement of the signal, respectively. Interferometers for GW detection are plagued primarily by displacement noise below 70 Hz and sensing noise above 200 Hz.

In the next sections I will describe briefly the specific types of displacement and sensing noises affecting the sensitivity of laser interferometers. A summary of the noise budget is shown in Fig. 3-1.

3.1.1 Displacement noise

ground motion, thermal noise

seismic noise physically displaces the mirrors, resulting in changes in the length of the arm.

3.1.2 Sensing noise

stray light, shot noise

Figure 3-1. Noise budget place holder.

Shot noise is a quantum mechanical effect of the detection of photons which creates uncertainty in the phase of the light, and therefore the power, at the AS port.

3.2 Measuring GW strain with light

3.2.1 Light as a photon

Consider two wave packets leaving the beam splitter of a Michelson interferometer at the same time, each heading down a different arm. If an appropriately polarized gravitational wave is present, the amount of time the wave packet takes to travel down a stretched arm and back is:

$$t_{rt+} = \frac{2L}{c}\left(1 + \frac{h_+}{2}\right) \tag{3.2.1}$$

Likewise, for a compressed arm the roundtrip travel time is:

$$t_{rt-} = \frac{2L}{c}\left(1 - \frac{h_+}{2}\right) \tag{3.2.2}$$

There is a non-zero $2Lh_+/c$ difference in arrival times at the beam splitter, a quantity one could measure with an accurate stationary clock. This demonstrates intuitively that a laser interferometer can detect gravitational waves.

It should be noted that we had to use the approximation that the gravitational wave wavelength λ_{gw} is much larger than the interferometer arm length L. This means that the temporal variation of $h_+(t)$ is negligible during the time it takes the photon to make its roundtrip. Thus, h_+ is treated as a constant in Eqs. 3.2.1 and 3.2.2.

3.2.2 Light as a wave

The detector at the beam splitter is not a clock, but a photodetector which is sensitive to phase. It would be informative, therefore, to express the difference in arrival times as a difference in phase. To do so, we must move away from the photon model and think about the wave model of light. The light wave's phase is given by $\phi = \omega t$ where t is the proper time. Then, the difference in phase between the two light beams after each has completed its roundtrip is:

$$\Delta\phi = \phi_{rt+} - \phi_{rt-} = \frac{2L\omega}{c}h_+ \tag{3.2.3}$$

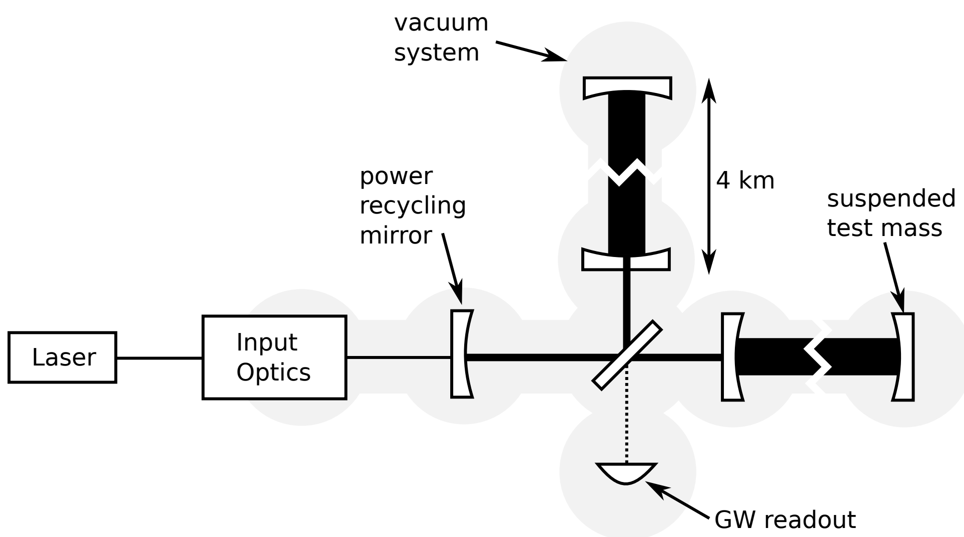

Figure 3-2. Power-recycled Fabry-Perot Michelson laser interferometer.

Two time derivatives yields

$$\frac{d^2\Delta\phi}{dt^2} = \frac{2L\omega}{c}\partial_t\partial_t h_+. \tag{3.2.4}$$

It can be shown [15] that the Riemann tensor in the TT gauge is $R_{tkti} = -\frac{1}{2}\partial_t\partial_t h_{ki}$, and gauge invariant. Therefore, our physically measurable quantity can be expressed as being manifestly gauge invariant, proving that a laser interferometer can detect the effect of gravitational waves.

3.3 Power-recycled Fabry-Perot Michelson interferometers

The typical detector configuration is a power-recycled Fabry-Perot Michelson laser interferometer featuring suspended test masses in vacuum as depicted in Figure 3-2. A diode-pumped, power amplified, and intensity and frequency stabilized Nd:YAG laser emits light at 1064 nm. The laser is directed to a Michelson interferometer whose two arm lengths are set to maintain destructive interference of the recombined light at the anti-symmetric (AS) port. An appropriately polarized gravitational wave will differentially change the arm lengths, producing signal at the AS port proportional to the GW strain and the input power. The Fabry-Perot cavities in the Michelson arms and a power recycling mirror (RM) at the symmetric port are two modifications to the Michelson interferometer that increase the laser power in the arms and therefore improve the detector's sensitivity to GWs.

- degrees of freedom
- phase detection, sidebands
- sub-systems, basic loops
- DARM

3.4 Controlling the interferometer

The ability of the interferometer to provide a differential arm length signal depends on the many interferometer cavities being locked all at once. It is the light, after all, that serves as our probe of arm length. However, the motion of the mirrors is too large for this state to naturally occur. For example, the rms pendular displacement of the mirrors without control is 1 μm, equivalent to a full laser wavelength. The arm length would swing from one free spectral range to the next, never staying put long enough for resonance to occur and for light from the arm to make its way to the anti-symmetric port.

The motion of the interferometer must be controlled enough such that resonance is achieved and so that error signals fall in a linear regime. Control does not improve the strain sensitivity, but it makes the strain measurement possible. The strain is determined by undoing the (carefully measured) effect of the control system on the differential arm length error signal.

Design considerations for the control loops include how much motion at what frequencies can be tolerated, and the signal to noise ratio of the motion sensor.

3.4.1 Digital Control in LIGO

The physical components of the LIGO interferometers are interfaced through a digital control system.

3.4.2 Mirror actuation

Each mirror is equipped with four optical sensor and electro-magnetic (OSEM) actuators for providing control to the mirror. Magnets arranged to form the four corners of a square are glued on the mirror's back surface, and the OSEM units envelop them. Length control of the cavities, for instance, sends current of the same magnitude through each coil on a given mirror to provide a piston force for changing the mirror's position.

3.5 More Laser Power

Shot noise results from an uncertainty in the arrival time of photons on a detector:

$$P_{shot} = \sqrt{2 h_p \nu P_{DC}} \text{ W}/\sqrt{\text{Hz}} \tag{3.5.1}$$

where P_{DC} is the DC power on the wavefront sensor, h_p is Planck's constant and ν is the frequency of the laser light.

CHAPTER 4
INPUT OPTICS

Insert IO paper here.

CHAPTER 5
ASC INTRODUCTION

5.1 Introduction

For the interferometer to first achieve lock and then remain at its linear operating point, the mirrors need to point at one another and remain stationary with respect to this pointing. In practice, however, the mirrors move around due to three torques inputs to each mirror: the suspension, the actuators, and radiation pressure. Each torque produces an angular displacement of the mirror as governed by the mirror's torque to angle transfer function and results in either a static or dynamic misalignment.

The dynamic misalignments arise from torque introduced through the suspension from ground motion and through the actuators from an unbalanced piston force. Both of these torques create an angular motion independent of the state of the mirror's pointing. Radiation pressure torque, however, stands apart; its effect depends on the pointing of the mirror. A consequence is that even when all of the mirrors are perfectly aligned at all frequencies, the simple existence of light in the interferometer makes the arm cavities statically unstable when high enough laser powers are used.

This chapter discusses the causes of mirror angular displacement and the effects of residual mirror motion on the interferometer. Background material is provided as necessary, such as the dynamics of torsion pendula, and the geometric eigenfunctions of linear cavities. In all, I hope to convince the reader of the need for an Angular Sensing and Control subsystem.

5.2 Overview of interferometer alignment

The interferometer alignment can be thought of in two basic units: the input beam and the power recycled Fabry-Perot Michelson. The alignment of the latter is nearly self-contained and can in fact be compacted down to a representative single mirror. The two remaining jobs are to align the input beam and this "single mirror" to one another and to keep the y-arm perpendicular to the x-arm.

The self-contained alignment of the power recycled Fabry-Perot Michelson is realized through a set of wavefront sensors (WFS). The pitch and yaw motions of the five mirrors in this unit, ETMX, ETMY, ITMX, ITMY, and the PRM, are sensed by the pitch and yaw of five WFS signals, WFS1Q, WFS2I, WFS2Q, WFS3I, and WFS4I, where I and Q denote in-phase and quadrature demodulation, respectively. These WFS look at light at the AS port, at the reflected port, and in the power recycling cavity. They control the relative motions of these five mirrors up to a couple Hz.

The MMT-directed input beam and the interferometer "mirror" need to be aligned so that the input beam is perfectly reflected upon itself. The input beam follows the interferometer on about minute time scales, and at higher frequencies the interferometer follows the input beam. The low frequency matching of the input beam pointing to the interferometer "mirror" is realized through the pitch and yaw signals of QPDX, a QPD which monitors the position of the light transmitted through the x-arm, and the pitch and yaw signals of a camera that monitors the beam location on the beam splitter. These two alignment sensors adjust the pointing of MMT1 and MMT3 on about minute time scales. An example of the BS camera image is shown in Fig. 5-1. The higher frequency matching of the input beam pointing to the interferometer is achieved by the reflected port Fabry-Perot Michelson wavefront sensors, up to a couple Hz.

The one additional step needed for full interferometer alignment is to maintain the orthogonality of the y-arm to the x-arm as the x-arm and input beam together move around. This is accomplished through the pitch and yaw signals of QPDY, the QPD that monitors the light transmitted through the y-arm, which sense how the beam splitter should be pointed. [1]

All mirror angles are of course interdependent and they must track each other. However, a rough hierarchy of who follows who can be established since ultimately the interferometer is bolted to the ground and necessarily maintains some DC orientation. This orientation comes from QPDX and QPDY, which are physically attached to piers standing on the ground and force

[1] QPDX also sends a signal to the BS to compensate for whatever it has MMT3 do.

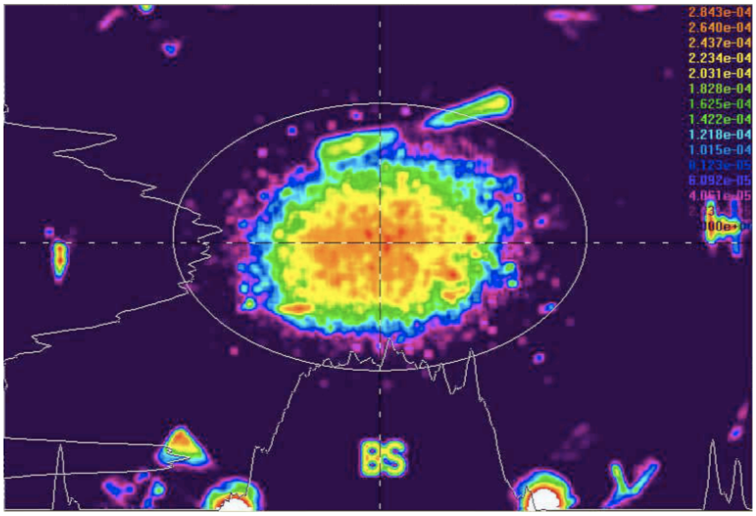

Figure 5-1. Image of beam on beam splitter as used in the beam centering servo. The beam appears stretched because the camera's viewing angle is at 45° with respect to the mirror surface. The color scale is arbitrary.

the beams transmitted through the ETMs to stay put at a certain location on their sensors. In all, the input beam must make it to those two exact places and the other mirrors are left to line themselves up accordingly. A diagram of this alignment scheme is in Fig. 5-2.

This alignment process involving the WFS, QPDs, and BS camera relies on the entire interferometer already being locked. It manages the continuous fine-tuning of mirror angles so that maximal power buildup in the interferometer is maintained, and so that the interferometer does not wander from its linear operating point. How to achieve the initial alignment of all of the mirrors is an interesting process in itself and is documented in Appendix 10.3.

5.3 Sources of mirror motion

If the interferometer can be aligned well enough by hand for the initial lock to be achieved, one might wonder why the need for continuous tweaking thereafter. The answer is that there is a continuous stream of changing torque inputs to the mirrors that cause them to twist and turn in pitch and in yaw. Some torque inputs exist regardless of the state of the interferometer, while others are a direct consequence of the control systems. The primary torque inputs are introduced here, and further discussion of some of them is found later in the chapter. The list includes:

- ground motion

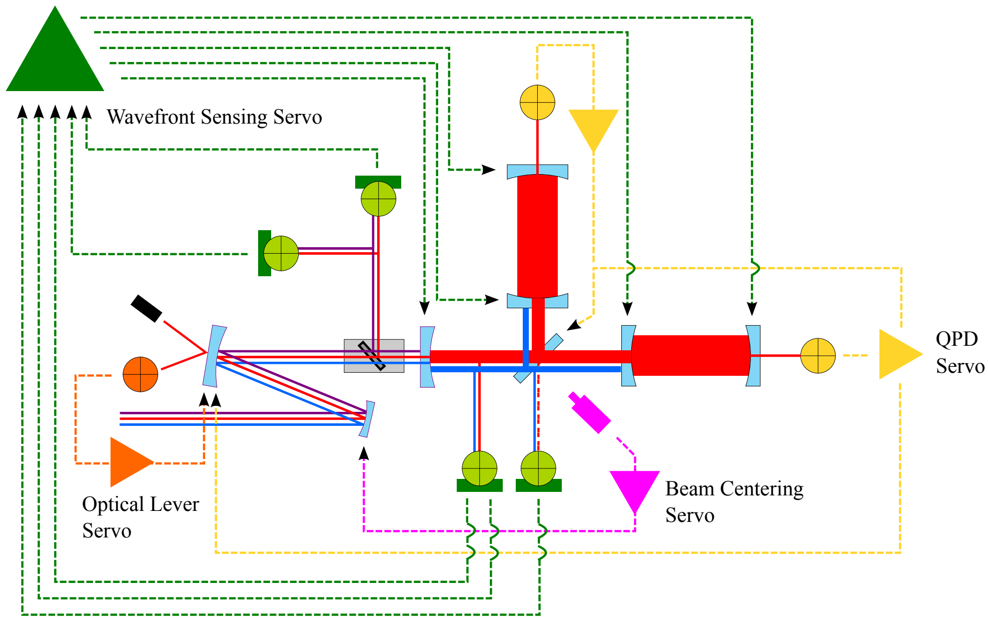

Figure 5-2. Schematic of the alignment sensing and control system, showing the placement of sensors and which mirrors they control. The QPD servo and Beam Centering Servo (BCS) together direct the input beam to follow the FPM unit on minute time scales. The QPD servo additionally keeps the BS properly directing light into the y-arm. The wavefront sensing servo maintains the alignment of the FPM mirrors with respect to each other up to several Hz. Each of the seven large optics has its own velocity damping optical lever servo.

- coil actuators (length to angle)
- radiation pressure
- noise impression from the angular control system

5.3.1 Ground motion

The most aggregious of these torque inputs is ground motion that makes its way through the multiple stages of seismic isolation to the mirror suspensions. This is the only source of angular motion that is present regardless of the state of interferometer operation, and it is also AC damped at all times for each of the large optics through optical lever witnesses. Keeping the mirrors quiet enough with respect to their local ground is necessary to allow for the initial locking of the interferometer, so each suspended optic, small and large, is quieted by its OSEM signals during the initial locking stages. An example of the shape and amount of velocity-damped angular motion experienced by the core optics due to seismic noise during a relatively quiet time

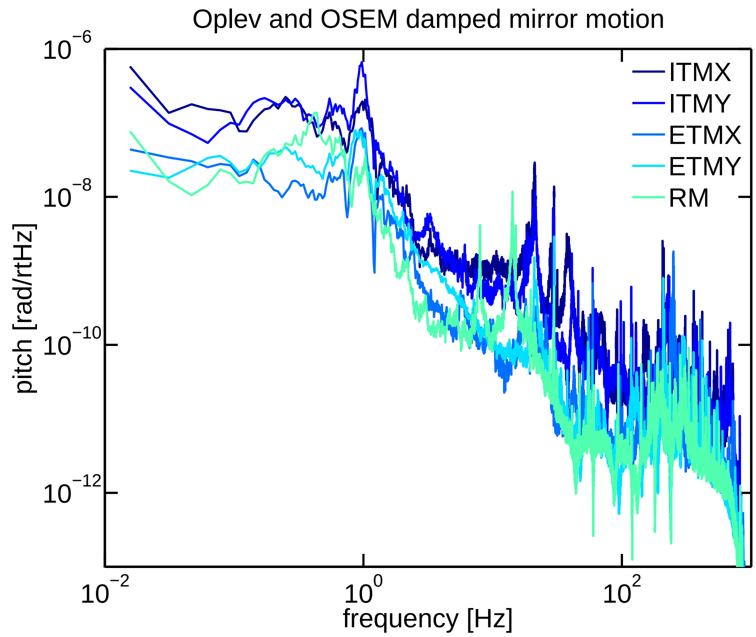

Figure 5-3. Typical angular motion of the core suspended mirrors in the absence of interferometric control. Velocity damping provided by the OSEMs?? and the optical levers is present. Once the interferometer is locked, the OSEM damping is ramped off.

is shown in Fig. 5-3. The rms mirror motion is of the order 10^{-7} rad. This is the motion that needs to be controlled interferometrically.

5.3.2 Coil actuators

The imperfect piston drive of the actuators on the rear of the test masses due to length control is another torque input, albeit inconsequential. The length of the cavities is carefully controlled (that's what we strive to be most sensitive to!) and any imbalances between the four electromagnets on a single mirror will create a coupling from length drive to angle (L2A). This effect is measurable, but is carefully tuned out through selecting appropriate digital gains for each of the coils. Typically, the gain variation from unity is up to 10%. The residual is about 1%. For the typical rms length drive of 1 μmon a core optic and osems separated by a distance of $\sqrt{2}R$ where R is the radius of the optic, the 1% L2A coupling results in a 10^{-8} radian displacement:

$$\theta = \frac{0.01 * 10^{-6}\ \mathrm{m}}{\sqrt{2} * 0.125\ \mathrm{m}} \approx 10^{-8}\ \mathrm{rad}. \tag{5.3.1}$$

5.3.3 Radiation pressure

Radiation pressure creates a torque when the beam impinges the mirror off-center. The force on the mirror due to radiation pressure is derived from the change in momentum of a photon upon reflection off the mirror and results in:

$$F_{rp} = \frac{2P}{c} \tag{5.3.2}$$

where P is the power of the light reflected by the mirror and c is the speed of light. Assuming the beam of photons strikes the mirror perpendicular to its surface, the torque exerted on a mirror due to radiation pressure is

$$\tau_{rp} = \frac{2Px}{c} \tag{5.3.3}$$

where x is the distance of the beam from the mirror's center of mass. For a 40 kW beam 1 mm off-center, the torque is on the order of 10^{-7} Nm, corresponding to an angular displacement of the order 10^{-7} rad as determined by the pendulum torque to angle transfer function (see 6.2).

Amongst the various torque inputs, radiation pressure plays a unique role in mirror motion because the torque it exerts depends on the angles of the mirrors. This is a result of the geometric coupling between beam displacements and mirror angles as will be shown in the next chapter. Radiation pressure therefore acts as an angular spring. It is best treated not as an external torque, but as a modification to the pendulum torque to angle transfer function. Part of the next chapter dedicates a discussion to this matter. In all, radiation pressure shapes the angular dynamics of the mirrors in LIGO and plays an important role in the design of an angular control system.

5.3.4 Noise from angular control

The angular control system, which strives to counteract the above torque inputs to reduce angular motion, introduces angular mirror motion itself. The primary way it contributes noise is through imperfect sensing of the angular displacements. The control system also impresses input beam motion on the mirrors. These issues and others are explained in more detail in 5.5.

5.4 Tolerance for angular motion

The requirements for how much motion is tolerable stem from two effects of misalignment that directly couple to strain sensitivity: power build-up degradation, and angle to length coupling. The misalignment tolerances are dictated by what is necessary to prevent the strain sensitivity of the perfectly aligned interferometer from degrading by more than 0.5% in the detection band of 40-7000 Hz [16].

Since the strain sensitivity is proportional to the power buildup (see Eq. **??**), a decrease in circulating power directly results in a decrease of shot-noise-limited DARM. Differing power fluctuations in the two arm cavities results in a changing contrast defect, a difference in the amount of light returning from one arm compared to the other, which increases the shot noise at the AS port. Too large of power fluctuations in the power recycling cavity makes for inconsistent signal to noise ratios for the signals that depend on sideband power. To maintain a power buildup within 1% of maximum, the core optics must have an angular displacement of less than 10^{-8} rad rms with respect to the cavity axis [17]. The derivation of power buildup as a function of mirror angle displacement is found in Appendix 10.2.

When the beam is located a distance x away from the center of the mirror, an angular displacement of the mirror θ about its center results in a path length change of the beam

$$\Delta L = x * \theta \tag{5.4.1}$$

which has a direct impact on DARM. Therefore, the alignment specifications must include not only tolerable levels of angular motion, but requirements for the physical centering of the beam spots on the mirrors. As detailed in Ref. [17], the beams must be centered on the core optics within 1 mm. At DC, for x $= 1$ mm and $\theta = 10^{-7}$ rad, $\Delta L = 10^{-10}$ m which is four orders of magnitude below the DARM rms of 10^{-6} m. Convolve my bsm spectra and residual mirror motion spectra to show example.

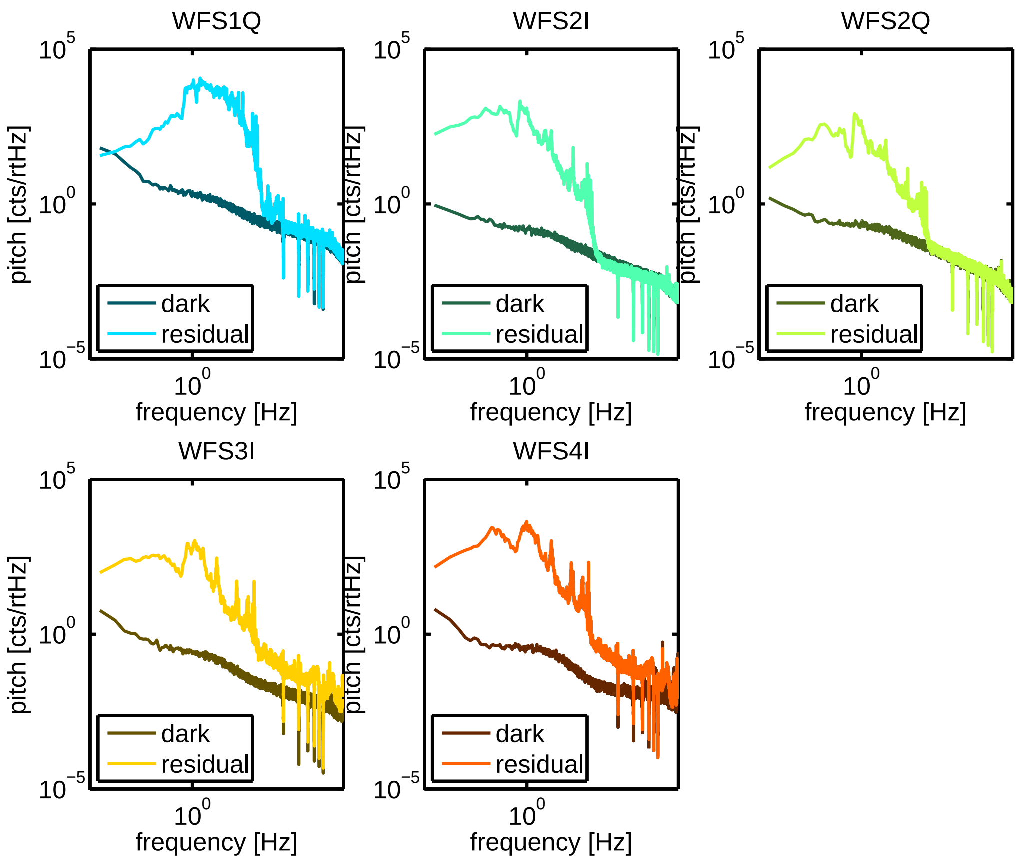

Figure 5-4. WFS sensor noise budget. Include shot noise, too, especially for WFS1. The excess signal above the dark noise in WFS3I and WFS4I from 20 Hz on is likely acoustic noise, although this has not been verified. WFS1 and WFS2 are on a floating table in a sound proof chamber, while WFS3 and WFS4 are on a non-seismically isolated table without a sound proof enclosure.

5.5 Angular control limitations

The limits for how good we can do in controlling the angular motion of the interferometer are governed by how well we are able to sense the angular motion. Several of the wavefront sensors' signals are dark-noise-limited above 20-25 Hz, as seen in Fig. 5-4. And depending on the power level, WFS1Q may instead be limited by shot noise (see Eq. 3.5.1). Any control signal derived from frequencies in the sensing noise limited regime will impress the sensor noise on the mirrors. This cannot be avoided entirely in the presence of feedback, but can be mitigated by including amongst the control filters a steep cut-off beginning at the sensor noise frequencies.

Besides the sensing noise, there is also sometimes real signal that results in more harm than good when used as feedback. The HAM seismic isolation tables used by the Input Optics (the core optics are suspended from BSC tables) have stack modes of xx Hz that ring up the MMTs. At low frequencies, around 1 Hz, some of the WFS signals are dominated by these angular fluctuations of the input beam. The resulting attempt of the mirrors to follow the input beam jitter leads to a magnification of the motion because of the drastically different length scales. Large power fluctuations in both arms and the power recycling cavity ensue, leading to departure from the linear error signal regime and often lock loss.

Other limitations to the reduction of mirror motion result from the nature of control loops. The cut-off filter, for example, reduces the phase margin of the open loop gain, necessarily pushing down the unity gain frequency (UGF) and therefore the magnitude of suppression at all frequencies below the UGF. A less aggressive cut-off filter, while improving the servo's stability and allowing for higher overall gains, leads to more impression of sensing noise on the optics. Also, when the phase margin of the loop is low, some mirror motion is amplified through gain peaking.

CHAPTER 6
DYNAMIC RESPONSE OF COUPLED PENDULA

6.1 Introduction

In order to design a control system that reduces the angular motion of the interferometer mirrors to the levels necessary for stable interferometer operation and minimal impact on strain sensitivity, the angular response of the mirrors to external torque must be fully understood. The suspended mirrors themselves are nothing more than torsion pendula. However, the torque induced by radiation pressure couples the angular motion of the mirrors in a power dependent way, complicating the plant for which controls must be designed. Namely, radiation pressure torque has the effect of breaking the symmetry of the equations of motion of each of the mirrors. Since Enhanced LIGO embarks on the path of increasing the laser power, examining the effect of radiation pressure torque in detail is warranted. Here, we review the dynamics of a torsion pendulum and the geometry of a linear cavity, and conclude with the derivation and implications of a set of eigenfunctions that diagonalize the linear cavity's response to radiation pressure. The torque to angle transfer functions of the new eigenmodes are modified such that one mode is statically unstable at Enhanced LIGO powers.

6.2 The mirror as a torsion pendulum

The mirrors in LIGO are torsion pendula. They are suspended from a single xx m diameter wire that makes contact with the bottom of the barrel of the mirror as shown in Fig. 6-1. Stand-offs glued just below the mirror's center of mass on both sides of the barrel mark the final point of contact of the wire with the mirror, and both ends of the wire are clamped to the top of a suspension cage. The mirror is free to twist an angle θ about a horizontal axis passing through its center of mass to create motion in *pitch* and about a vertical axis passing through its center of mass to create a motion in *yaw*.

The angular equation of motion of the mirror is governed by the sum of all torques on the mirror. First, let's consider the most simplistic scenario where there is only a pendulum restoring

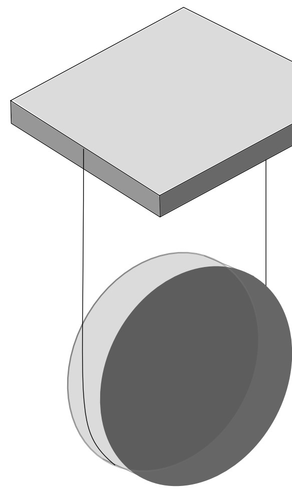

Figure 6-1. Cartoon of a LIGO suspension. Improve this.

torque $\tau_p = -\kappa_p \theta$, where κ_p is the pendulum's torsional constant. The equation of motion is

$$I\ddot{\theta} + \kappa_p \theta = 0, \tag{6.2.1}$$

which has a solution of $\theta(t) = \sin(\omega_0 t)$, where $\omega_0 = \sqrt{\kappa_p/I}$ is the resonant angular frequency and I is the mirror's moment of inertia. The pendulum torsional constant serves to make the mirror oscillate indefinitely about its equilibrium position upon the slightest of displacements.

6.2.1 Torque to angle transfer function of a pendulum

We are particularly interested in the pendulum's response to an external torque, such as seismic noise. In order to calculate the torque to angle transfer function, we must include an external torque term, τ_{ext}, in the equation of motion:

$$I\ddot{\theta} + \gamma\dot{\theta} + \kappa_p \theta = \tau_{ext}. \tag{6.2.2}$$

Here, we have also introduced a velocity damping term, γ, to best model reality. Taking the Laplace transform to convert from the time domain to the frequency domain, we have:

$$Is^2\Theta + \gamma s\Theta + \kappa_p \Theta = \tau_{ext} \tag{6.2.3}$$

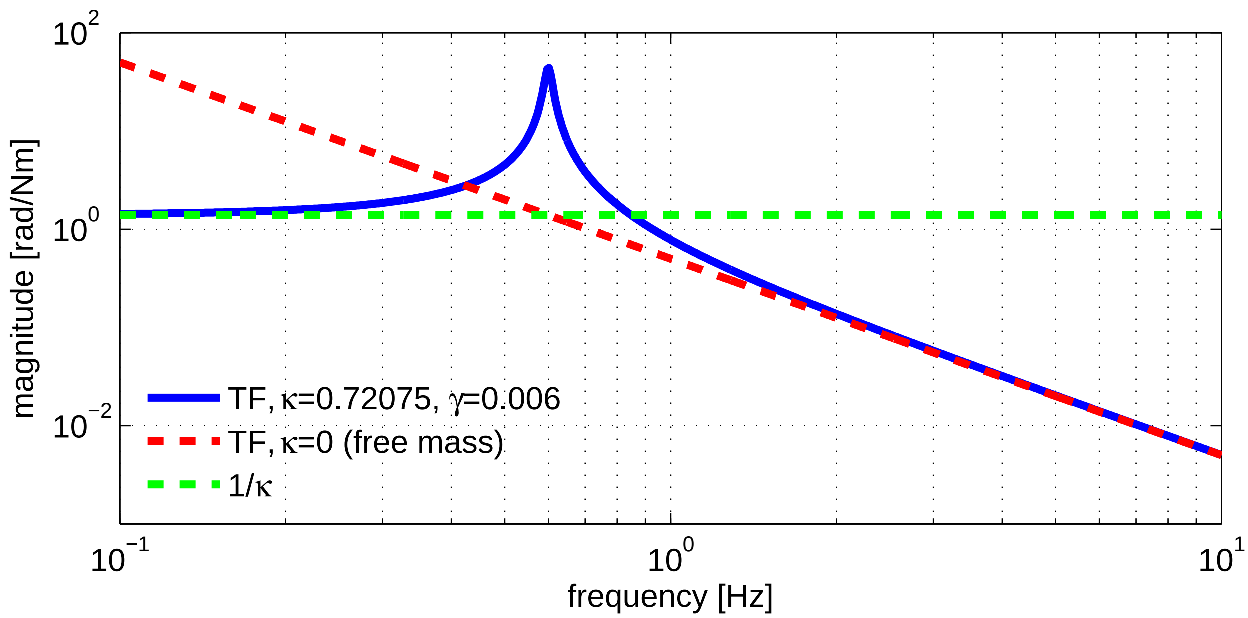

Figure 6-2. Torque to pitch transfer function of a LIGO core optic (blue). The optic acts like a free mass at high frequencies (green) and the DC magnitude of the transfer function is determined by the inverse torsional constant (red). A damping constant $\gamma = 0.006$ ($Q = 32$) was selected for pictorial reasons only. The resonant frequency of LIGO core optics in yaw is 0.5 Hz.

where s is a complex parameter. We are only interested in examining the transfer function for a pure sine wave excitation, $e^{i\omega t}$, so we substitute $s = i\omega$ to get

$$\mathrm{TF} := \frac{\Theta}{\tau_{ext}} = \frac{1}{Is^2 + \gamma s + \kappa_p} = \frac{1/I}{\omega_0^2 - \omega^2 + i\gamma\omega/I}. \tag{6.2.4}$$

A more familiar quantity to use than γ for describing the losses of a system with a real resonance is the quality factor, $Q := \omega_{res}/\mathrm{FWHM}$, where FWHM is that computed for the amplitude squared of the transfer function. When the losses are small, $\omega_{res} \approx \omega_0$ and FWHM $\approx \gamma/I$ (see Feynman 23-4). The quality factor is then well approximated by $Q = \sqrt{\kappa_p I}/\gamma$. The transfer function written in terms of Q is

$$\mathrm{TF} = \frac{1/I}{\omega_0^2 - \omega^2 + i\omega\omega_0/Q}. \tag{6.2.5}$$

Figure 6-2 shows the pendulum torque to angle transfer function (for pitch) using the parameters of a LIGO core optic. For external torques applied to the mirror above its resonant frequency, the mirror acts like a free mass, one that is not held in place by suspension wires nor subject to damping. For torques applied to the mirror below its resonant frequency, the mirror's angle is determined by the inverse of the torsional constant.

6.3 The radiation pressure angular spring

The geometric axis of a cavity formed by two spherical mirrors is dictated by the line joining the centers of the "spheres" created by the two mirrors. Only if the mirrors are pointed directly at one another will the cavity axis pass through the centers of the mirrors. Should a laser beam resonate in the cavity, it will do so along this geometric axis. Thus, if the mirrors are tilted away from one another, the beam spot on each mirror will not be centered. The relationship between the positions of the beams on the mirrors relative to center, x_i, and the angles of the mirrors, θ_i, is given by:

$$\begin{bmatrix} x_1 \\ x_2 \end{bmatrix} = \frac{L}{1-g_1g_2} \begin{bmatrix} g_2 & 1 \\ 1 & g_1 \end{bmatrix} \begin{bmatrix} \theta_1 \\ \theta_2 \end{bmatrix}. \tag{6.3.1}$$

The g-factor is defined as $g_i = 1 - R_i/L$ where R_i is the radius of curvature of each of the mirrors, respectively, and L is the length of the cavity.

We saw in the previous chapter that the radiation pressure torque on a mirror depends on the position of the beam on the mirror, $\tau_{rp} = 2Px/c$ (Eq. 5.3.3). Based on Eq. 6.3.1 the radiation pressure torque on a mirror that is part of a Fabry-Pérot cavity is therefore dependent on the angle of both the mirror of interest and the second mirror forming the cavity:

$$\begin{bmatrix} \tau_{rp,1} \\ \tau_{rp,2} \end{bmatrix} = \frac{2PL}{c(1-g_1g_2)} \begin{bmatrix} g_2 & 1 \\ 1 & g_1 \end{bmatrix} \begin{bmatrix} \theta_1 \\ \theta_2 \end{bmatrix}. \tag{6.3.2}$$

This is more succinctly expressed as

$$\vec{\tau}_{rp} = -\mathbf{K_{rp}}\vec{\theta}, \tag{6.3.3}$$

where $\mathbf{K_{rp}}$ is the *torsional stiffness matrix*. Equation 6.3.3 is the expression that describes the radiation pressure angular spring.

6.3.1 Diagonalizing the modified equations of motion

The radiation pressure spring modifies the pendulum angular equation of motion and therefore the torque to angle transfer function, through the addition of an angle-dependent torque term. Re-writing Eq. 6.2.2 in matrix form and with the radiation pressure spring term, the two equations that describe the motion of two mirrors forming a Fabry-Pérot cavity is:

$$\mathbf{I}\ddot{\vec{\theta}} + \gamma\dot{\vec{\theta}} + \kappa_{\mathbf{p}}\vec{\theta} - \frac{2PL}{c(1-g_1g_2)} \left[\!\!\left[\begin{array}{cc} g_2 & 1 \\ 1 & g_1 \end{array} \right]\!\!\right] \vec{\theta} = \vec{\tau}_{ext}. \tag{6.3.4}$$

$\mathbf{I}$, γ, and κ_p are 2×2 diagonal matrices and $\vec{\theta}$ and $\vec{\tau}_{ext}$ are 2×1 vectors as in the previous section. Due to the non-diagonal matrix in Eq. 6.3.4, the motions of each of the mirrors forming the cavity are tied to one another. The natural way to work with such a system is to rotate the coupled equations into a new basis. The resulting de-coupled equations of motion will described specific combinations of mirror tilts instead of individual mirrors. Vectors in the rotated basis are written with primes.

In order to decouple the two equations of Eq. 6.3.4, we need to diagonalize $\mathbf{K_{rp}}$. The subscripts a and b are used to denote the elements of the diagonalized basis, to contrast the 1 and 2 which denote the mirror basis. Ignoring the constants of matrix $\mathbf{K_{rp}}$, its eigenvalues are

$$\lambda_a = \frac{g_1 + g_2 + \sqrt{(g_1-g_2)^2+4}}{2} \tag{6.3.5}$$

$$\lambda_b = \frac{g_1 + g_2 - \sqrt{(g_1-g_2)^2+4}}{2} \tag{6.3.6}$$

and its eigenvectors are

$$\vec{v}_a = \left[\!\!\left[\begin{array}{c} 1 \\ \frac{g_1-g_2+\sqrt{(g_1-g_2)^2+4}}{2} \end{array} \right]\!\!\right] \tag{6.3.7}$$

$$\vec{v}_b = \left[\!\!\left[\begin{array}{c} \frac{-g_1+g_2-\sqrt{(g_1-g_2)^2+4}}{2} \\ 1 \end{array} \right]\!\!\right]. \tag{6.3.8}$$

Therefore, the matrix

$$\mathbf{S} = \begin{bmatrix} \vec{v}_a & \vec{v}_b \end{bmatrix} = \begin{bmatrix} 1 & \frac{-g_1+g_2-\sqrt{(g_1-g_2)^2+4}}{2} \\ \frac{g_1-g_2+\sqrt{(g_1-g_2)^2+4}}{2} & 1 \end{bmatrix} \tag{6.3.9}$$

diagonalizes $\mathbf{K_{rp}}$ such that

$$\mathbf{S^{-1}K_{rp}S} = \mathbf{D} = \begin{bmatrix} \lambda_a & 0 \\ 0 & \lambda_b \end{bmatrix} = \begin{bmatrix} \frac{g_1+g_2+\sqrt{(g_1-g_2)^2+4}}{2} & 0 \\ 0 & \frac{g_1+g_2-\sqrt{(g_1-g_2)^2+4}}{2} \end{bmatrix}. \tag{6.3.10}$$

The matrix of eigenvectors, $\mathbf{S}$, is the basis transformation matrix. It serves to define the torque and angle vectors in the new basis. For example,

$$\vec{\theta}' = \begin{bmatrix} \theta_a \\ \theta_b \end{bmatrix} = \mathbf{S^{-1}} \begin{bmatrix} \theta_1 \\ \theta_2 \end{bmatrix} = \mathbf{S^{-1}}\vec{\theta}. \tag{6.3.11}$$

Rearranging Eq. 6.3.10 to the form $\mathbf{K_{rp}} = \mathbf{SDS^{-1}}$ and substituting it into Eq. 6.3.4, we have:

$$\mathbf{I}\ddot{\vec{\theta}} + \gamma\dot{\vec{\theta}} + \kappa_{\mathbf{p}}\vec{\theta} - \frac{2PL}{c(1-g_1g_2)}\mathbf{SDS^{-1}}\vec{\theta} = \vec{\tau}_{ext} \tag{6.3.12}$$

Multiplying on the left by $\mathbf{S}$, taking advantage of the diagonal $\mathbf{I}$, γ, and κ_p matrices, and using $\mathbf{S}$ to change the basis of each of the vectors, the de-coupled equations of motion are:

$$\mathbf{I}\ddot{\vec{\theta}}' + \gamma\dot{\vec{\theta}}' + \kappa_{\mathbf{p}}\vec{\theta}' - \frac{2PL}{c(1-g_1g_2)} \begin{bmatrix} \lambda_a & 0 \\ 0 & \lambda_b \end{bmatrix} \vec{\theta}' = \vec{\tau}'_{ext}. \tag{6.3.13}$$

The radiation pressure spring constant, κ_{rp}, is

$$\kappa_{rp} = -\frac{2PL}{c(1-g_1g_2)}\lambda \tag{6.3.14}$$

where $\lambda = \lambda_a$ or λ_b, depending on the mode in question.

The angular motion of the Fabry-Pérot cavity is no longer described on an individual mirror basis. Due to radiation pressure, the cavity is treated as a unit and the two orthogonal modes of angular motion are combinations of the two mirrors' angles. The eigenvectors $\vec{v}_a$ and $\vec{v}_b$ describe

Table 6-1. Geometric parameters of the LIGO arm cavity eigenmodes. x_i are the beam locations on the mirrors relative to center, a is the cavity axis displacement at the waist, and α is the cavity axis angle with respect to a line joining the centers of the mirrors. Differences between LLO and LHO arise from the mirrors at each site having different radii of curvature. Quantities are expressed as a function of the amount of tilt in a particular mode.

cavity parameter	unit	LLO $\vec{v}_a$ mode	LLO $\vec{v}_b$ mode	LHO $\vec{v}_a$ mode	LHO $\vec{v}_b$ mode
$\lvert x_1 \rvert$	mm/urad	9.88	2.44	8.20	2.51
$\lvert x_2 \rvert$	mm/urad	10.84	2.22	9.35	2.20
$\lvert a \rvert$	mm/urad	10.17	1.01	8.48	1.34
$\lvert \alpha \rvert$	urad/urad	0.24	1.17	0.29	1.18

these two sets of orthogonal mirror tilts, and the eigenvalues λ_a and λ_b (along with their common constants) quantify the magnitude of the radiation pressure torsional spring constant for each of the modes. While the equations of motion had been identical for each of the individual mirrors, the decoupled equations in the presence of radiation pressure breaks that symmetry.

Table 6-1 outlines the characteristics of these two eigenmodes for the specific geometry of the LIGO arm cavities. The amount of beam displacement on each mirror is given as a function of the amount of tilt in one eigenmode or the other. Furthermore, the amount of cavity axis displacement a and cavity axis tilt α is also calculated for each eigenmode using the geometric relationship between a set of mirror tilts and their cavity axis as derived in Appendix 10.1. Figure 6-3 illustrates a cavity in each of the two eigenmodes when using the parameters from Table 6-1.

6.3.2 Soft and hard modes

The torque to angle transfer function of each of these eigenmodes has the same form as that of a single pendulum (Eq. 6.2.4), but the spring constant is modified. More importantly, the spring constant is modified differently for each mode, yielding distinct behaviors of the two eigenmodes. In this section, we analyze these behaviors and accordingly introduce the names *soft* and *hard* to use in place of a and b for describing the two modes.

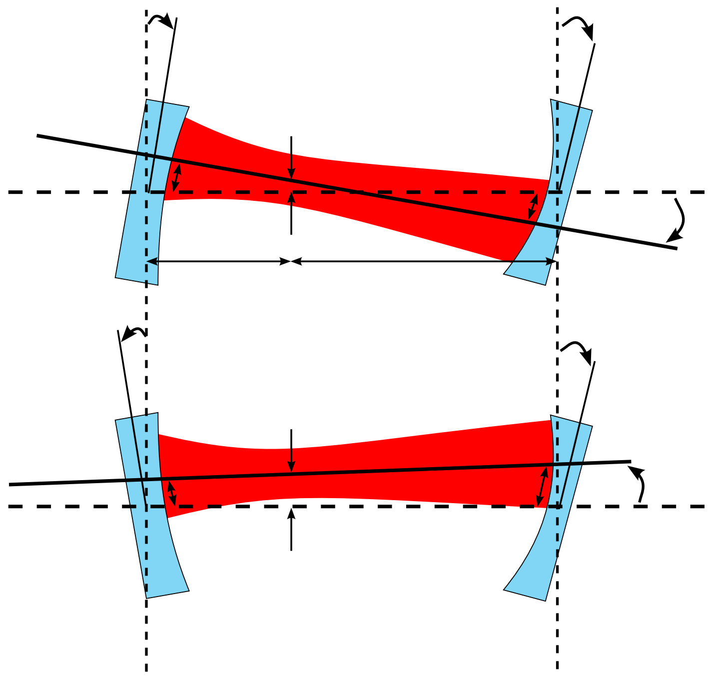

Figure 6-3. Illustration of the orthogonal modes of cavity tilt. The upper diagram shows tilts given by eigenvector $\vec{v}_b$ and the lower diagram shows $\vec{v}_a$. Labels.

Just as in Sec. 6.2.1, we can take the Laplace transform of each of the equations in Eq. 6.3.13 to get the general form of the modal torque to angle transfer function:

$$\frac{\Theta'}{\tau'_{ext}} = \frac{1}{Is^2 + \gamma s + \kappa_p + \kappa_{rp}}. \tag{6.3.15}$$

Figure 6-4 shows the control theory view of the addition of the radiation pressure spring constant to the transfer function.

The magnitude and sign of the total torsional spring constant, $\kappa_{tot} = \kappa_p + \kappa_{rp}$, conveys critical information about the stability of the cavity and the nature of its response to external torque. Recalling the equation of an angular spring, $\tau = -\kappa_{tot}\theta$, a restoring torque is provided only if $\kappa_{tot} > 0$, which is equivalent to the condition for stability. If $\kappa_{tot} < 0$, the spring serves to amplify the angle, resulting in an unstable, run-away situation. Furthermore, while κ_{tot} is positive, its magnitude directly relates to the stiffness of the spring.

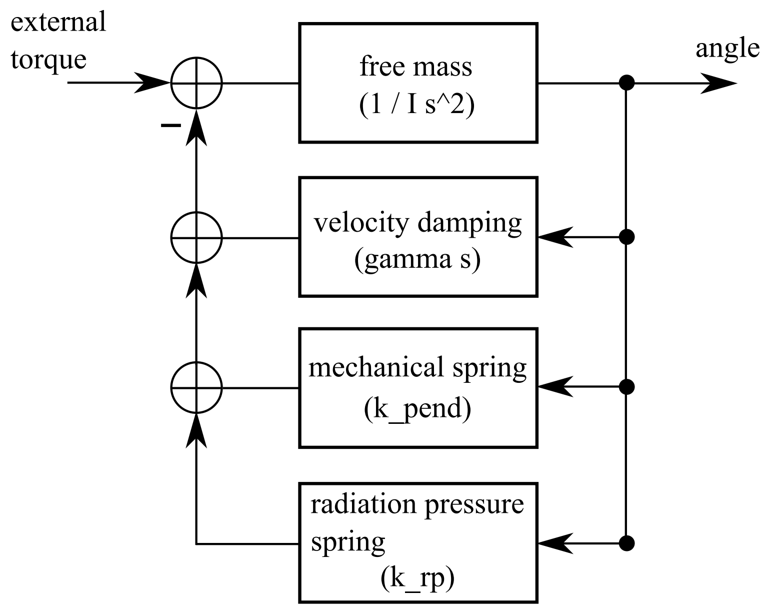

Figure 6-4. Demonstration of how radiation pressure modifies the torque to angle transfer function of a Fabry-Pérot cavity's eigenmodes.

The stability criteria for the coupled cavity eigenmodes depend on the relationship between κ_p and κ_{rp}:

$$\text{stable: } k_{tot} > 0 \implies \frac{2PL}{c(1-g_1g_2)}\lambda < \kappa_p \tag{6.3.16}$$

$$\text{unstable: } k_{tot} < 0 \implies \frac{2PL}{c(1-g_1g_2)}\lambda > \kappa_p. \tag{6.3.17}$$

The pendulum spring constant, κ_p, is always positive, so we can conclude with certainty that the cavity eigenmode is stable as long as the quantity on the left-hand side of Eq. 6.3.17 is negative. However, if this quantity is positive, then its magnitude compared to κ_p determines stability. Since P, L, and c are all positive numbers and the g-factor is restricted to $0 < g_1g_2 < 1$ [1] , the sign of the left-hand side is determined solely by that of λ. From the g-parameter restriction, it can be shown that λ_a is always positive and that λ_b is always negative. Therefore, the mode whose

[1] This is the necessary condition for a two mirror resonator to form a stable periodic focusing system. [18, p. 747]

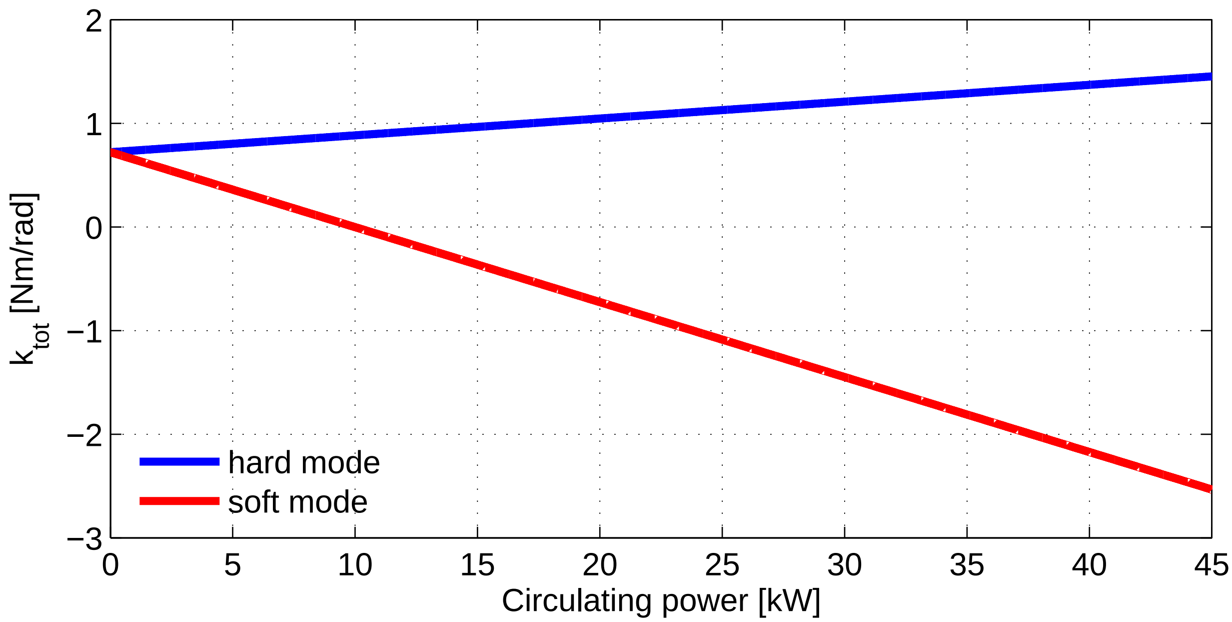

Figure 6-5. Torsional spring constants (pitch) of an optically coupled cavity for LLO parameters. The soft mode is unstable when the spring constant is negative.

mirror angles are described by $\vec{v}_a$ is either stable or unstable, and the mode described by $\vec{v}_b$ will always be stable.

The precise situation for the potentially unstable mode depends on the one non-constant variable, the circulating power P. There is a critical power at which κ_{rp} = - κ_p, and at any greater power, instability ensues. In general, as power increases, the total spring constant for the potentially unstable mode decreases, creating a softer spring, and the total spring constant for the unconditionally stable mode increases, creating a stiffer spring. Thus arise the terms *soft* and *hard* to describe the two eigenmodes that have been referred to by $\vec{v}_a$ and $\vec{v}_b$, respectively.

Figure 6-5 shows the dependence of κ_{tot} on circulating power for the soft and hard modes of a LIGO arm cavity. Without power in the cavity, the modes are identical and their spring constants are simply that of the individual pendula. The symmetry-breaking effect of radiation pressure comes into play as soon as light resonates in the cavity: the hard mode's spring constant increases and the soft mode's spring constant decreases. The critical power at which the soft mode becomes unstable is 10 kW, which corresponds to approximately 6 W input power (for Enhanced LIGO efficiencies) to the interferometer. Table 6-2 highlights the values of the spring

Table 6-2. Torsional spring constants (pitch) for the soft and hard modes of a typical Initial LIGO power and the highest of Enhanced LIGO powers. The soft mode in Enhanced LIGO is unstable.

	P_{circ}	κ_p	κ_{tot}, soft mode	κ_{tot}, hard mode
Initial LIGO	9 kW	0.721 Nm/rad	0.0734 Nm/rad	0.867 Nm/rad
Enhanced LIGO	40 kW	0.721 Nm/rad	-2.18 Nm/rad	1.38 Nm/rad

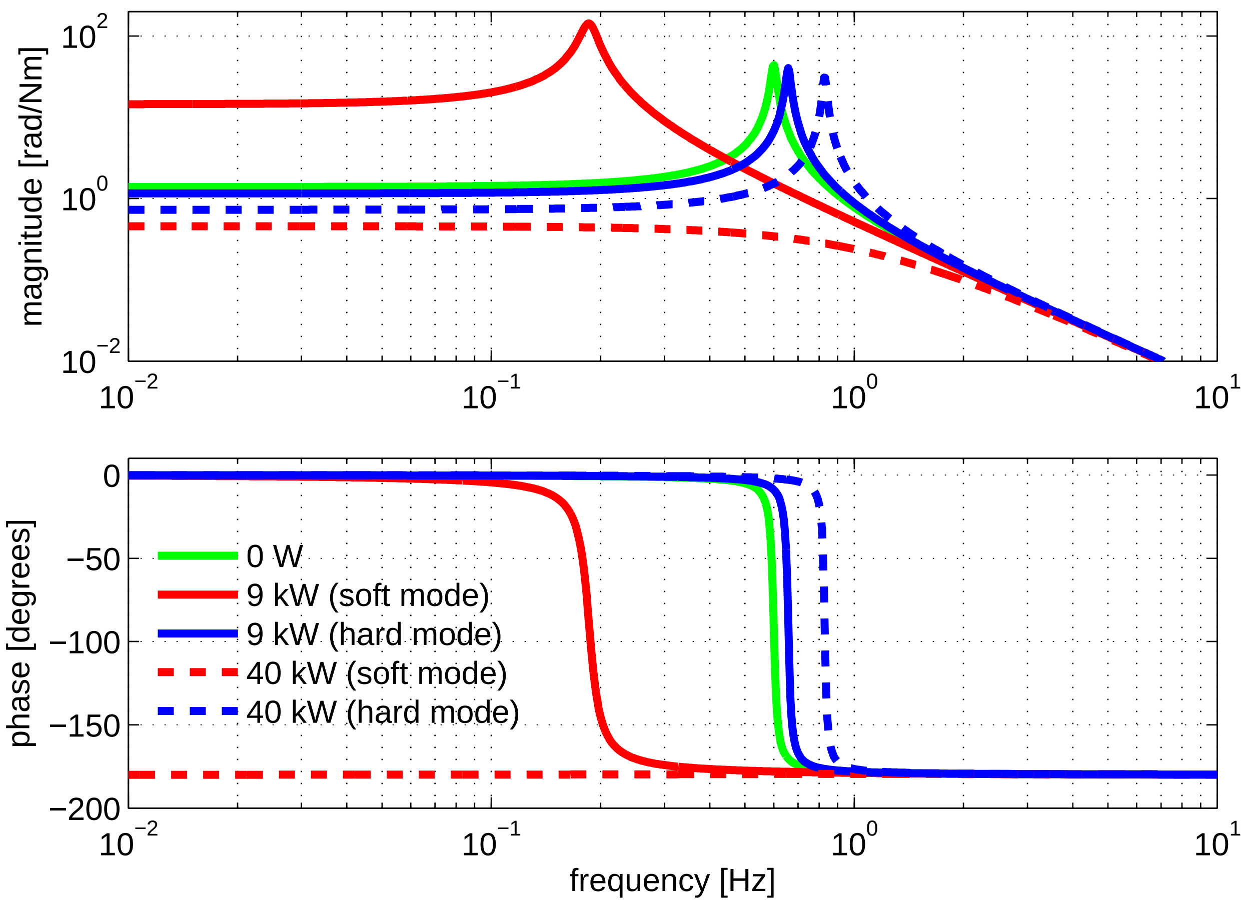

Figure 6-6. Single cavity opto-mechanical transfer function for pitch. The resonant frequency increases with power for the hard mode, but decreases for the soft mode, eventually becoming imaginary. $P_{circ} = 9$ kW (5.25 W input) was a typical operating power for Initial LIGO and $P_{circ} = 40$ kW (23.5 W input) is the highest of powers reached for Enhanced LIGO.

constants for the typical power used in Initial LIGO and for the highest of powers achieved in Enhanced LIGO, and the transfer functions for these spring constants is found in Fig. 6-6. The resonant frequency, $\omega_0 = \sqrt{\kappa_{tot}/I}$, increases with power for the hard modes and decreases for the soft modes. These are the transfer functions for which controls must be designed.

CHAPTER 7
SENSING AND CONTROLLING MIRROR MOTION IN THE RADIATION PRESSURE EIGENBASIS

7.1 Introduction

The Enhanced LIGO goal of increasing the input power to 30 W from the Initial LIGO 7 W makes radiation pressure torques cross into the realm of significance. In particular, the soft opto-mechanical mode which approached instability for Initial LIGO powers actually becomes unstable for Enhanced LIGO powers. The static instability requires high DC gain. The sensors in Initial LIGO, however, were not tuned in to specifically look for the combined mirror motions that create the unstable mode. The only way to provide adequate DC control to prevent the mirrors from falling apart would be to increase the gain of all of the angular control loops. Since some of the sensors are less good than others, this would result in extreme impression of noise on DARM. Thus, to maintain a reasonable noise budget while reigning in the static instability, we need to make the sensors specifically pick out the mirror motions that together create this detrimental mode. This is the basis of the ASC work for Enhanced LIGO–switching the sensors to the radiation pressure eigenmode basis, and increasing the gain of the single loop that is sensitive to only the unstable mode.

In this chapter I show how the angular displacements are sensed and why control filters implemented in the eigenbasis of radiation pressure torques is best.

7.2 Sensor noise and noise contribution to DARM

7.3 Solving the noise problem with the eigenbasis

7.4 ASC to DARM noisebudget

The cut-off frequency of the lowpass filters for the WFS control are of particular importance in the DARM noisebudget. The lowpass filter is necessary for suppressing the impression of sensing noise on suspension control.

7.5 Beam spot motion

- calibration

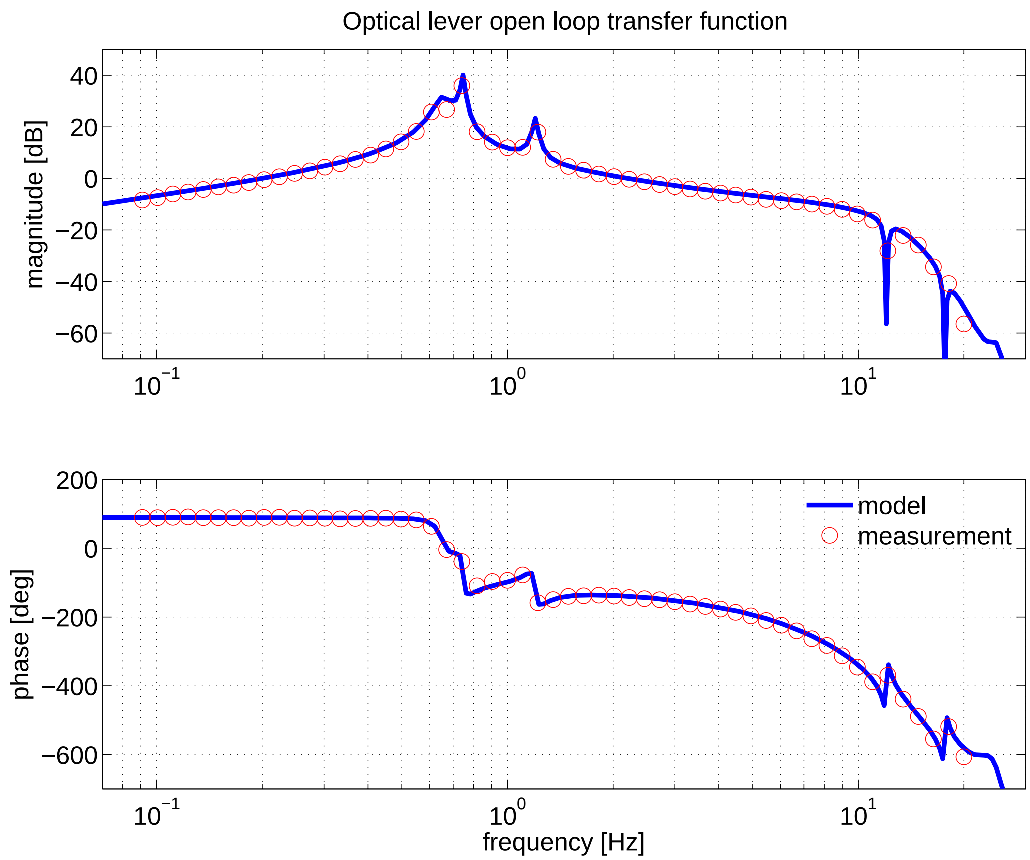

Figure 7-1. ETMX optical lever open loop transfer function. Uses the filters in the oplev servo filter bank, only (no coil output filters). The model of the plant is tuned to match the data, resulting in a pitch resonance of 0.65 Hz and a damping factor of $\gamma = 0.02$. The UGF is at 2.2 Hz and the phase margin is 38°.

- residuals, perhaps for different kinds of seismic

7.6 Heating related measurements

- effect of PRC g-parameter on ASC sensing matrix
- SPOB power scaling

7.7 DC readout related measurements

- RF created from DC offset beam moving on WFS1
- RF vs DC vs power comparison of (AS) beam spot motion on WFS1

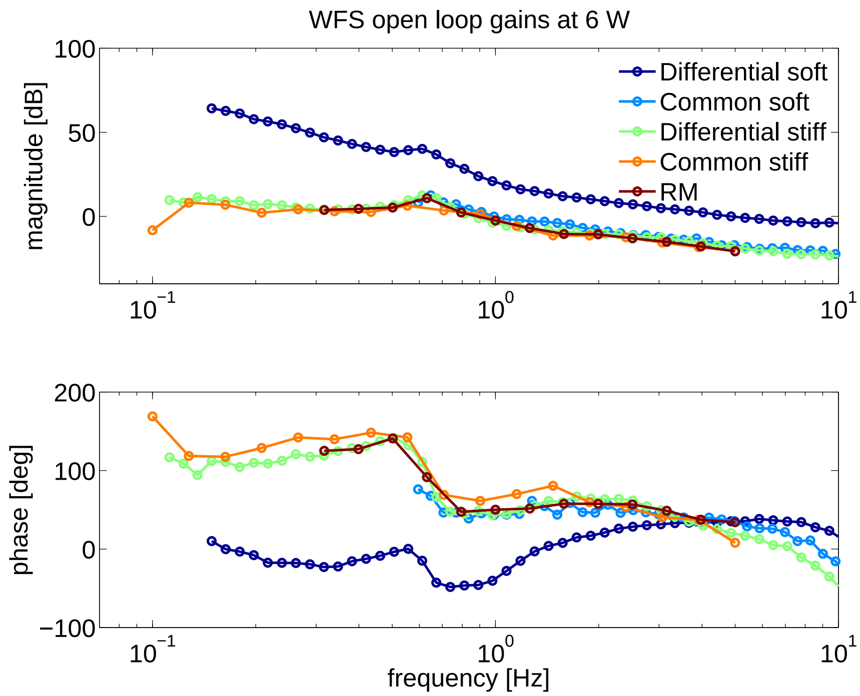

Figure 7-2. Pitch open loop gains of the 5 WFS loops as measured with 6 W input power.

7.8 ASC noisebudget

- seismic - breakdown of soure of motion
- L2A
- input beam
- electronics noise
- shot noise

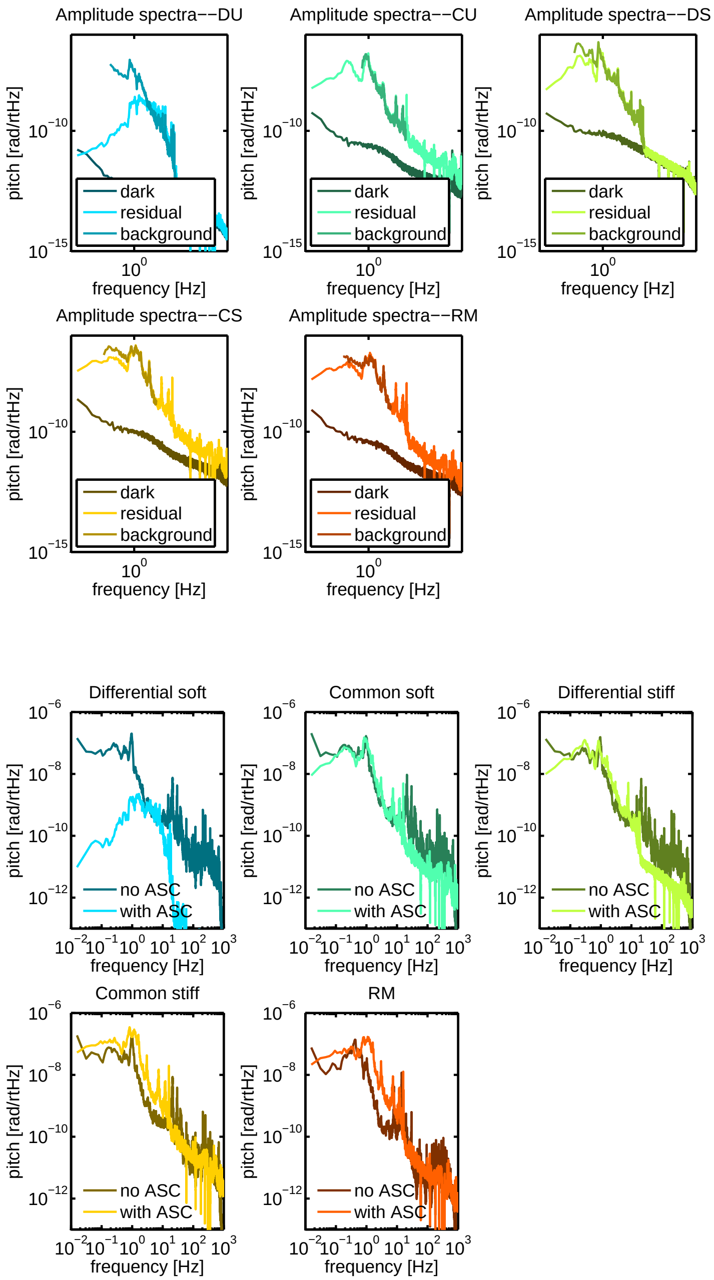

Figure 7-3. Top: Comparison of motion with and without the ASC. Eigenbasis residual during 10 W lock, and background derived from loop correction. Completely different day from bottom plot. Bottom: Propagation of sensor signals from 10 W lock through input matrix and power scaling to eigenbasis, compared with eigenbasis reconstruction of optical lever signals when interferometer not locked, but optics under oplev damping. Data are taken 45 minutes apart.

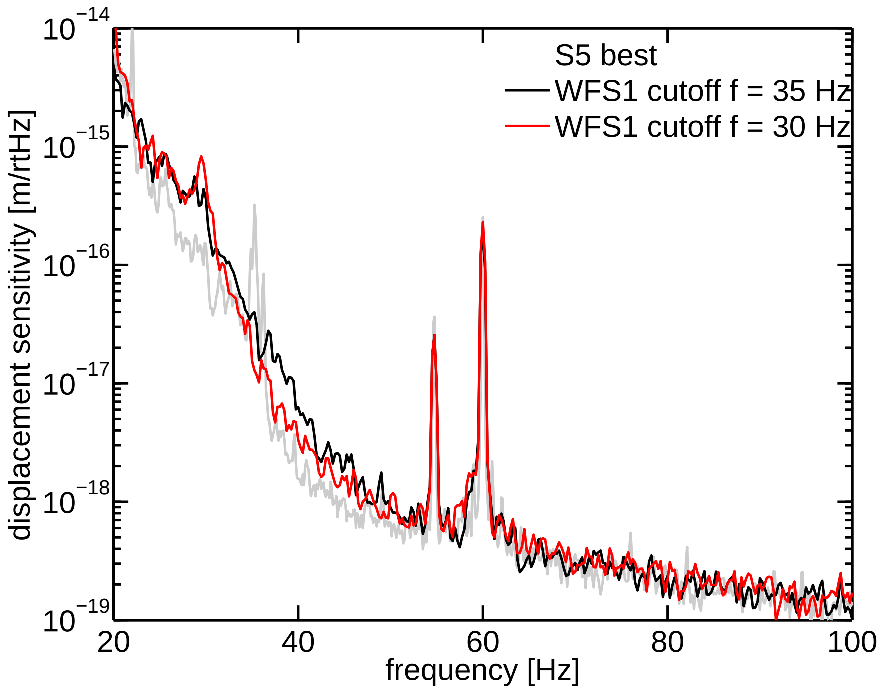

Figure 7-4. Effect of the WFS1 lowpass filter cutoff frequency on strain sensitivity.

CHAPTER 8
EXPERIMENTAL MEASUREMENT OF THE SIDLES-SIGG EFFECT

8.1 Measured modes

CHAPTER 9
SUMMARY

469.75502pt

Figure 9-1. Reflected beam from the Advanced LIGO pre-mode cleaner.

CHAPTER 10
APPENDIX

10.1 Misaligned cavity axis

Here I provide the geometric argument that shows how to calculate the tilt a and displacement α of a cavity as a function of mirror misalignment. Cavity tilt is defined by the angle formed between the line that connects the two beam spots (as given by Eq. 6.3.1) and the line joining the centers of the mirrors. Cavity displacement uses the same two lines, yet is defined by the distance between them at the location of the waist of the resonant spatial mode. Based on pure geometry, the cavity displacement and tilt are:

$$\begin{bmatrix} a \\ \alpha \end{bmatrix} = \frac{1}{L} \begin{bmatrix} z_2 & z_1 \\ -1 & 1 \end{bmatrix} \begin{bmatrix} x_1 \\ x_2 \end{bmatrix} \tag{10.1.1}$$

where z_i is the distance to the waist from mirror i calculated as:

$$z_1 = \frac{g_2(1-g_1)L}{g_1+g_2-2g_1g_2} \tag{10.1.2}$$

$$z_2 = L - z_1. \tag{10.1.3}$$

Clearly, we can combine Eqs. (6.3.1) and (10.1.1) to arrive at an equation directly relating mirror tilt to cavity displacement and tilt:

$$\begin{bmatrix} a \\ \alpha \end{bmatrix} = \frac{1}{1-g_1g_2} \begin{bmatrix} g_2z_2+z_1 & z_2+g_1z_1 \\ -g_2+1 & -1+g_2 \end{bmatrix} \begin{bmatrix} \theta_1 \\ \theta_2 \end{bmatrix}. \tag{10.1.4}$$

10.2 Power in a misaligned cavity

I'll show how to calculate the power in a cavity as a function of cavity axis displacement and tilt. Combined with the results of Eq. 10.1.4 we determine how the power build-up in a cavity depends on a single mirror's angular displacement.

The field of a lowest-order Gaussian laser beam along one axis at the beam waist is:

$$\psi(x) = U_0(x) = \left[\frac{2}{\pi w_0^2}\right]^{1/4} \exp\left[-\left[\frac{x}{w_0}\right]^2\right] \tag{10.2.1}$$

where w_0 is the beam waist radius and U_0 is the lowest-order Hermite polynomial. The Hermite polynomials are orthonormal, ie. $\langle U_i \mid U_j \rangle = \delta_{ij}$. For example, the next to lowest order polynomial is:

$$U_1(x) = \left(\frac{2}{\pi w_0^2}\right)^{1/4} \frac{2x}{w_0} \exp\left[-(x/w_0)^2\right] = \frac{2x}{w_0} U_0(x) \tag{10.2.2}$$

10.2.1 Displaced cavity

The field of a cavity with a *displaced* z-axis at the cavity waist is:

$$\begin{aligned} \psi\prime(x) =& \psi(x-a) && (10.2.3) \\ =& U_0(x-a) && (10.2.4) \\ =& c_0 U_0(x) + c_1 U_1(x) + c_2 U_2(x) + \ldots && (10.2.5) \\ & && (10.2.6) \end{aligned}$$

where a is the displacement of the axis and c_i are constants.

10.2.1.1 Power

We want to know c_0, the projection of the displaced cavity field onto the beam field:

$$\begin{aligned} c_0 &= \langle \psi \mid \psi\prime \rangle && (10.2.7) \\ &= \int_{-\infty}^{\infty} \psi(x) \psi\prime(x)\, dx && (10.2.8) \\ &= \exp\left[-a^2/2w_0^2\right] && (10.2.9) \end{aligned}$$

The power in this mode is the square of the overlap of the two fields:

$$\begin{aligned} P_0 &= |\langle \psi \mid \psi\prime \rangle|^2 && (10.2.10) \\ &= \exp\left[-[a/w_0]^2\right] && (10.2.11) \end{aligned}$$

10.2.1.2 U_1 field

For the purpose of wavefront sensing, we need to know the amplitude, c_1, of the first order U_1 field. This can be approximated as demonstrated in Anderson [19] using the Taylor series expansion of the exponential in $\psi\prime(x) = U_0(x-a)$, assuming a displacement a that's small compared to waist size w_0.

$$\begin{aligned}
\psi\prime(x) &= \left[\frac{2}{\pi w_0^2}\right]^{1/4} \exp\left[-\left[\frac{x-a}{w_0}\right]^2\right] && (10.2.12)\\
&= \left[\frac{2}{\pi w_0^2}\right]^{1/4} \left[1-\left[\frac{x-a}{w_0}\right]^2+\mathscr{O}(a^4)\right] && (10.2.13)\\
&= \left[\frac{2}{\pi w_0^2}\right]^{1/4} \left[\frac{2xa}{w_0^2}\left[1-\frac{x^2}{w_0^2}+\ldots\right]+\left[1-\frac{x^2}{w_0^2}+\frac{1}{2}\frac{x^4}{w_0^4}-\ldots\right]+\mathscr{O}(a^2)\right] && (10.2.14)\\
&= \left[\frac{2}{\pi w_0^2}\right]^{1/4} \left[1+\frac{2xa}{w_0^2}+\mathscr{O}(a^2)\right] \exp\left[-\left[\frac{x}{w_0}\right]^2\right] && (10.2.15)\\
&= U_0(x)+\frac{a}{w_0}U_1(x)+\ldots && (10.2.16)
\end{aligned}$$

Notice that here we find $c_0 = 1$, which is consistent with the exact result of Eq. 10.2.9 when we apply our $a^2 \approx 0$ approximation. We find that the amplitude of the first order Hermite-Gauss field for a displaced cavity is

$$c_1 = a/w_0. \qquad (10.2.17)$$

10.2.2 Tilted cavity

The field of a cavity with a *tilted* z-axis at the cavity waist is a tad more complex to derive. We assume the tilt, α, is small such that $\sin\alpha \approx \alpha$ and $\cos\alpha \approx 1$. Also, we assume the beam divergence angle, $\theta_0 = \lambda/\pi w_0$, is small such that the wavefronts near the waist can be considered parallel to one another.

Here, the important quantity to consider is the phase of the cavity field at the cross-section of the beam waist. The phase is either advanced or retarded compared to that of the beam:

$$\begin{aligned}
\psi\prime(x) &= \psi(x\prime)\exp[-ikz\prime] && (10.2.18)\\
&\approx \psi(x\cos\alpha)\exp[-ikx\sin\alpha] && (10.2.19)\\
&\approx \psi(x)\exp[-ikx\alpha] && (10.2.20)\\
&= U_0(x)\exp[-ikx\alpha] && (10.2.21)
\end{aligned}$$

where $k = 2\pi/\lambda$ and λ is the wavelength of the laser light.

10.2.2.1 Power

The overlap of the fields of the beam and tilted cavity is $\exp[-\alpha^2/2\theta_0^2]$. Therefore the power is:

$$P_0 = \exp[-(\alpha/\theta_0)^2]. \tag{10.2.22}$$

10.2.2.2 U_1 field

An expansion of the exponential in Eq. 10.2.21 for a small tilt α gives:

$$\begin{aligned} \psi\prime(x) &= U_0(x)[1 + ikx\alpha + \mathscr{O}(\alpha^2)] & (10.2.23) \\ &= U_0(x) + \frac{ik\alpha w_0}{2} U_1(x) + \mathscr{O}(\alpha^2). & (10.2.24) \end{aligned}$$

Therefore, the amplitude of the first order Hermite-Gauss field for a tilted cavity is

$$c_1 = ik\alpha w_0/2. \tag{10.2.25}$$

10.2.3 Displaced and tilted cavity

The most general case, of course, is to have a cavity axis that is both displaced *and* tilted at the beam waist:

$$\psi\prime(x) = \psi(x-a)\exp[-ik(x-a)\alpha]. \tag{10.2.26}$$

We find:

$$\langle \psi \mid \psi\prime \rangle = \exp\left[-\frac{a^2}{2w_0^2}\right]\exp\left[-\frac{\alpha^2}{2\theta_0^2}\right]\exp\left[-\frac{ia\alpha}{x_0\theta_0}\right] \tag{10.2.27}$$

and

$$P_0 = \exp\left[-\frac{a^2}{w_0^2}\right]\exp\left[-\frac{\alpha^2}{\theta_0^2}\right]. \tag{10.2.28}$$

10.3 Initial DC alignment of the interferometer

After any kind of in-vacuum work, the DC alignment of the mirrors is usually too poor for the interferometer to lock. A bootstrapping process of tweaking the alignment by hand is necessary, assuming the mirrors start out pointing in generally the right direction, as is usually the case. As pointed out in 5.2, the QPDs at the end stations are the fixed reference points for the overall alignment, so this process begins with making sure the light reaches them. We then adjust the rest of the mirrors to maximize power build-up in the arms and to maximze spatial overlap of the light reflected from each arm.

An outline of the process is presented here. “Misalign” means to intentionally point a mirror so far away from any known good positions as to eliminate it from the configuration. “Align” and “restore” mean to bring a mirror or configuration to the best known position(s). Centering the beam on a mirror is accomplished by using the suspension cage surrounding the mirror as a reference. Camera images and QPD readback provide the signals used for beam centering.

X-arm

- restore the x-arm (misalign RM, ITMY, and ETMY, align ITMX and ETMX)
- use ITMX to center the beam on QPDX
- use ETMX to center the beam on ITMX
- with x-arm locked, use MMT3 to maximize the x-arm power build-up (NPTRX, can expect about 95%)
- save the MMT3, ITMX, and ETMX alignment settings

Y-arm

- restore the y-arm (misalign ITMX and ETMX, align ITMY and ETMY)
- use ITMY to center the beam on QPDY
- use ETMY to center the beam on ITMY
- with y-arm locked, use BS to maximize the y-arm power build-up (NPTRY, can expect about 90%)
- save the BS, ITMY, and ETMY alignment settings

Relative x-arm and y-arm

- note AS beam position on camera while toggling between x-arm and y-arm locks
- use ETMs to align the two AS beams
- restore the Michelson (misalign ETMs, align ITMs)
- use BS to make AS port as dark as possible
- re-do y-arm alignment if ambitious

Recycling mirror

- restore the PRM (misalign ETMs, align ITMs and RM)
- use RM to center beam on ETMY cage

Restore full interferometer–off you go!

REFERENCES

[1] J. Sidles and D. Sigg, Physics Letters A **354**, 167 (2006), ISSN 03759601, URL http://dx.doi.org/10.1016/j.physleta.2006.01.051.

[2] E. Hirose, K. Kawabe, D. Sigg, R. Adhikari, and P. R. Saulson, Appl. Opt. **49**, 3474 (2010), URL http://dx.doi.org/10.1364/AO.49.003474.

[3] L. Barsotti and M. Evans, Tech. Rep. T080186, LIGO Laboratory (2009), URL https://dcc.ligo.org/cgi-bin/private/DocDB/ShowDocument?docid=6570.

[4] P. Linsay, P. Saulson, R. Weiss, and S. Whitcomb, Tech. Rep. T830001, Massachusetts Institute of Technology (1983).

[5] B. P. Abbott, R. Abbott, R. Adhikari, P. Ajith, B. Allen, G. Allen, R. S. Amin, S. B. Anderson, W. G. Anderson, M. A. Arain, et al., Reports on Progress in Physics **72**, 076901+ (2009), ISSN 0034-4885, URL http://dx.doi.org/10.1088/0034-4885/72/7/076901.

[6] F. Acernese, P. Amico, M. Alshourbagy, F. Antonucci, S. Aoudia, P. Astone, S. Avino, L. Baggio, G. Ballardin, F. Barone, et al., Journal of Optics A: Pure and Applied Optics **10**, 064009+ (2008), ISSN 1464-4258, URL http://dx.doi.org/10.1088/1464-4258/10/6/064009.

[7] H. Lück, M. Hewitson, P. Ajith, B. Allen, P. Aufmuth, C. Aulbert, S. Babak, R. Balasubramanian, B. W. Barr, S. Berukoff, et al., Classical and Quantum Gravity **23**, S71 (2006), ISSN 0264-9381, URL http://dx.doi.org/10.1088/0264-9381/23/8/S10.

[8] R. Adhikari, P. Fritschel, and S. Waldman, Tech. Rep. T060156, LIGO Laboratory (2006), URL https://dcc.ligo.org/cgi-bin/DocDB/ShowDocument?docid=7384.

[9] H. Lück, C. Affeldt, J. Degallaix, A. Freise, H. Grote, M. Hewitson, S. Hild, J. Leong, M. Prijatelj, K. A. Strain, et al., Journal of Physics: Conference Series **228**, 012012+ (2010), ISSN 1742-6596, URL http://dx.doi.org/10.1088/1742-6596/228/1/012012.

[10] Advanced LIGO Systems Group, Tech. Rep. T010075, LIGO Laboratory (2009), URL https://dcc.ligo.org/cgi-bin/DocDB/ShowDocument?docid=5489.

[11] T. Fricke, N. Smith, R. Abbott, R. Adhikari, K. Dooley, M. Evans, P. Fritschel, V. Frolov, K. Kawabe, and S. Waldman, in preparation (2011), URL https://dcc.ligo.org/cgi-bin/private/DocDB/ShowDocument?docid=8442.

[12] J. S. Kissel, Ph.D. thesis, Louisiana State University (2010).

[13] M. Frede, B. Schulz, R. Wilhelm, P. Kwee, F. Seifert, B. Willke, and D. Kracht, Opt. Express **15**, 459 (2007), URL http://dx.doi.org/10.1364/OE.15.000459.

[14] P. Willems, A. Brooks, M. Mageswaran, V. Sannibale, C. Vorvick, D. Atkinson, R. Amin, and C. Adams, *Thermal Compensation in Enhanced LIGO* (2009).

[15] D. Garfinkle (2005), gr-qc/0511083, URL http://arxiv.org/abs/gr-qc/0511083.

[16] P. Fritschel and D. Shoemaker, Tech. Rep. T952007, LIGO Laboratory (1997).

[17] I. Group, Tech. Rep., LIGO Laboratory (1998).

[18] A. E. Siegman, *Lasers* (University Science Books, 55D Gate Five Road, Sausalito, CA 94965, 1986).

[19] D. Z. Anderson, Appl. Opt. **23**, 2944 (1984), URL http://dx.doi.org/10.1364/AO.23.002944.

BIOGRAPHICAL SKETCH

Kate's biography.